



Article

Electrical Model Analysis for Bifacial PV Modules Using Real Performance Data in Laboratory

Valentina González Becerra ¹, Patricio Valdivia-Lefort ^{2,*} , Rodrigo Barraza ³ and Jesús García García ⁴ 

¹ Department of Electrical Engineering, Universidad Técnica Federico Santa María, Santiago 8940000, Chile; valentina.gonzalezbe@sansano.usm.cl

² Department of Electrical Engineering, Universidad de Santiago de Chile, Santiago 8370003, Chile

³ Faculty of Engineering and Sciences, Universidad Adolfo Ibáñez, Santiago 7941169, Chile; rodrigo.barraza@uai.cl

⁴ Institute of Mechanical Engineering, Faculty of Engineering Sciences, Universidad Austral de Chile, Valdivia 5110566, Chile; jesus.garciagarcia@uach.cl

* Correspondence: patricio.valdivia.l@usach.cl

Abstract: The new PV technologies, such as bifacial modules, bring the challenge of analyzing the response of numerical models and their fit to actual measurements. Thus, this study explores various models available in the literature for simulating the IV curve behavior of bifacial photovoltaic modules. The analysis contains traditional models, such as single and double-diode models, and empirical or analytical methodologies. Therefore, this paper proposes and implements a model performance assessment framework. This framework aims to establish a common basis for comparison and verify the applicability of each model by contrasting it with experimental data under controlled conditions of irradiance and temperature. The study utilizes bifacial modules of PERC+, HJT, and n-PERT technologies, tracing IV curves using a high-precision A+A+A+ solar simulator and conducting two sets of laboratory illumination measurements: single-sided and double-sided. In the first case, each face of the module is illuminated separately, while in the latter, the incident frontal illuminating light is reflected on a reflective surface. Experimental data obtained from these measurements are used to evaluate three different approximations for bifacial IV curve models in the case of double-sided illumination. The employed model for single-sided illumination is a single-diode model. The evaluation of various models revealed that shadowing from frames and junction boxes contributes to an increase in the error of modeled IV curves. However, among the three evaluated bifacial electrical models, one exhibited superior performance, with current errors approaching approximately 20%. To mitigate this discrepancy, a proposed methodology highlighted the significance of accurately estimating I_0 , suggesting its potential to reduce errors. This research provides a foundation for comparing electrical models to identify their strengths and limitations, paving the way for the development of more accurate modeling approaches tailored to bifacial modules. The insights gained from this study are crucial for enhancing the precision of IV curve predictions under various illumination conditions, which is essential for optimizing bifacial module performance in real-world applications.

Keywords: PV models; bifacial module; experimental data



Citation: González, V.; Valdivia-Lefort, P.; Barraza, R.; Sanchez-Squella, A.; García, J. Electrical Model Analysis for Bifacial PV Modules Using Real Performance Data in Laboratory. *Energies* **2024**, *17*, 5868. <https://doi.org/10.3390/en17235868>

Academic Editor: Francesco Nocera

Received: 7 October 2024

Revised: 4 November 2024

Accepted: 6 November 2024

Published: 22 November 2024



Copyright: © 2024 by the authors. Licensee MDPI, Basel, Switzerland. This article is an open access article distributed under the terms and conditions of the Creative Commons Attribution (CC BY) license (<https://creativecommons.org/licenses/by/4.0/>).

1. Introduction

Bifacial photovoltaic (PV) technology, in contrast to its monofacial counterparts, offers the unique capability of harnessing solar energy from both the front and rear sides of the PV module. This technology increased significance and is projected to capture a substantial 70% market share by 2030 [1]. The advantages of adopting bifacial PV technology over monofacial systems are diverse and compelling. First, the ability to capture light from both sides leads to notable gains in energy production [2–4]. Bifacial PV systems exhibit

enhanced energy yield by leveraging reflected light from the ground, surrounding surfaces, and even the sky. Second, the deployment of bifacial modules, even with a simple arrangement, contributes to a reduction in the levelized cost of energy. However, this cost reduction can be further optimized by utilizing increased albedo, emphasizing the importance of considering the reflective properties of the installation area [5]. Last, bifacial PV technology demonstrates its value for climate change since it could offer higher power outputs for future irradiance scenarios than monofacial PV, making them a promising choice for sustainable energy generation [6].

In this scenario, it is important to have reliable tools that can accurately predict the energy production of PV modules or arrangements under different environmental conditions. Since different locations have their own unique temperature levels, irradiance, humidity, and other factors, it is essential to consider these variables when modeling energy production. For that purpose, several electrical, thermal, and optical models have been developed to represent the behavior of PV devices. Considering that bifacial PV technology is relatively new, it is necessary to conduct more research to determine if electrical models are good enough to represent its behavior or if new modeling approaches are required to lead to more accurate predictions of energy production.

Several electrical models have been proposed to represent the behavior of bifacial PV modules, but their validation has predominantly relied on limited methods, as summarized in Table 1. Most studies have used outdoor measurements, which, although realistic, lack sufficient control over variables such as irradiance distribution and module temperature. Other studies turn to simulations, which, while useful for analyzing specific scenarios, may not fully capture the complexities of real-world conditions. Typical validation approaches focus on energy output and power comparisons between modeled and experimental results; however, an in-depth analysis of the IV curve remains crucial. This analysis allows for a more precise evaluation of parameter fitting and highlights potential discrepancies. Overall, the dependence on outdoor data and simulations for validating bifacial PV models presents significant limitations, underscoring the need for alternative, more controlled validation methods to achieve robust and reliable results.

Table 1. Proposed validation method.

Validation Method	Ref	Proposed Model	Evaluation Method	PV Device	Technology	Measurement Conditions
Outdoor measurement	[7]	Parallel single diode	IV curve	Cell	Not reported	Temperature: 25–55 °C. Irradiance: 1000 W/m ² .
				Module	Not reported	Albedo: 0.16. Irradiance: 900 ± 20 W/m ² .
Outdoor measurement	[8]	Double diode	Annual bifacial gain and energy output	Cell	N-type	Vertical east-west orientation. Two different albedo.
Outdoor measurement	[9]	Single and double diode	IV curve	Module	N-type	Frontal irradiance at 1000 W/m ² while rear irradiance varies between 0% and 30%.
Outdoor measurement	[10]	Single diode traditional and parallel configuration	Power and cumulative energy	Module	Not reported	Daily performance estimation, considering summer and winter days.
Outdoor measurement	[11]	Analytical and empirical	DC power	Monofacial and bifacial PV array	PERC	Variation in albedo levels Different levels of temperature and irradiance depending on weather conditions.
Simulation	[12]	Single diode	Energy yield	Module	Not reported	Daily and yearly performance estimation, considering sunny and cloudy days.
Simulation	[13]	Single diode	IV curves for monofacial and bifacial module	Module	Not reported	STC condition: 25 °C and 1000 W/m ² . 20 °C and 800 W/m ² .

This article provides a significant improvement over existing literature by assessing electrical models for bifacial PV technology using high-quality data obtained in an indoor solar simulator under controlled conditions. By conducting evaluations in this environment, the research achieves a more accurate and reliable assessment of various electrical models for bifacial PV modules than traditional methods, which often lack control over critical variables. The experimental data include IV curves from multiple PV modules, spanning different manufacturers and technologies, measured under meticulously managed irradiance and temperature conditions using an A+A+A+ Eternalsun solar simulator. This control over irradiance is essential, as PV modules are highly sensitive to the spectral distribution of solar irradiance [14], and variable conditions like cloud cover introduce prediction challenges [15]. By conducting the study in a controlled environment, the setup minimizes potential errors from the optical model and avoids noise related to clouds, reflections, and shading effects, offering a robust validation framework that addresses the limitations found in outdoor measurements.

This research seeks to identify the most accurate electrical model for bifacial PV technology. By comparing the simulated results of different models against meticulously collected indoor data, the research aims to discern which model best captures the complex behavior of bifacial modules. Additionally, the study aims to assess the sensitivity of the best electrical models to variations in electrical parameters, providing insights into the factors that significantly impact model accuracy. This study is structured into several key sections. It begins with a concise review of the indoor characterization of bifacial PV devices, followed by an examination of proposed bifacial models found in existing literature. The methodology section provides a detailed exposition of the experimental setup and the associated data processing methodologies. Subsequent sections present the results obtained from both single-sided and double-sided measurements. Finally, the study culminates with comprehensive conclusions drawn from the synthesis of gathered data and the analyses conducted throughout the investigation.

2. Characterization of Bifacial PV Devices

Characterization of PV devices provides relevant information regarding their performance, including max power rating, efficiency, estimation of annual energy yield, sizing of system components, and determination of product value [16]. Standard IEC 60904-1-2 [17] provides recommended electrical parameters for reporting and the corresponding measurement methods for bifacial PV devices. This overview will center on two types of illumination: single and double-sided. Specifically, the emphasis will be on indoor measurements, focusing on laboratory tests.

2.1. Single-Sided Illumination

When measuring IV curves on bifacial devices, one consideration is to illuminate only one side. The standard IEC 60904-1-2 specifies that the limit of irradiance on the non-illuminated side should be less than 3 Wm^{-2} . There are multiple methods available to achieve this requirement:

- Use a non-reflective material behind the non-illuminate side.
- Limit the exposure of the module illuminating with a source of the size of the module.
- Cover the non-illuminated side with a black surface.

Liang et al. [18] investigated the considerations outlined in the standard and devised an experimental setup comprising two distinct darkrooms. They aimed to generate varying background reflections to examine their impact on characterization results. Their findings revealed that the non-uniformity of irradiance influences two parameters: fill factor and maximum power. Moreover, irradiances exceeding 3 Wm^{-2} were found to introduce uncertainties to the maximum power measurements. It is important to carefully consider the conditions under which the rear surface is exposed during single-sided characterization to minimize the effects of reflections and non-uniform irradiance. Implementing the recommended methods from the standard is crucial in addressing these issues.

Razongles et al. [19] examined parasitic reflections occurring when the bifacial module is positioned away from the black screen surface to mitigate the effects above. They suggested placing a black screen directly on the back of the module to minimize reflections.

2.2. Double-Sided Illumination

In the case of double-sided illumination, it is crucial to accurately measure both frontal and rear irradiances and develop a method to illuminate both faces consistently. There are various arrangements and measurement techniques. For instance, Lagunas et al. [20] utilized a 10 ms pulse class-A flash simulator to illuminate the device, with two glasses and mirrors positioned at a 45° tilt from the direction of the light pulse. A mesh was employed to control rear face light. Irradiance was measured using a reference cell, while current and voltage were gauged using probes. This setup enabled distinct irradiance levels on each side of the PV device. Different scenarios were examined to compare the IV curve behavior when the device was illuminated separately from each side or simultaneously. Results revealed that simultaneous illumination from both sides led to a lower maximum power point than the sum of currents obtained under separate illumination conditions.

Zhang et al. [21] comprehensively compared one-sided and two-sided illumination. Their experimental setup involved a light source directed towards a bifacial cell and a white smooth plate capable of reflecting incident light. The same configuration was used for single-sided measurements, albeit with adjustments made to the distance between the laminates and the light source. They evaluated three different types of bifacial cells: n-type, p-type, and HJT. In contrast to the findings of Lagunas et al. [20], they observed that two-sided illumination resulted in higher levels of maximum power points than one-sided illumination.

Finally, Razongles et al. [19] implemented two indoor setups. The first is implemented for large modules, where two identical EternalSun sun simulators were located at each device surface. With this configuration, the irradiance can be totally controlled for both surfaces. The second setup utilized an aluminum-mirror arrangement specifically designed for 4-cell modules. This setup is very similar to the proposal of Lagunas et al., using a mesh as a filter to control the irradiance on the rear face.

Across the various presented setups, several commonalities emerge. Firstly, each setup utilizes reference cells to measure irradiance accurately. Additionally, there is a consistent practice of attenuating incident light on the rear face of the setup, emulating the albedo effect. These methodological consistencies serve as foundational pillars for the forthcoming exposition of our proposed setup, to be detailed in the Methodology section.

3. Bifacial Electrical Models

The electrical output of a PV device can be simulated using diverse models. One commonly employed approach is based on the single-diode formulation [22–27], which incorporates five parameters: photocurrent (I_{ph}), diode ideality factor (η), diode saturation current (I_s), series resistance (R_s), and shunt resistance (R_{sh}) [28]. However, as the single-diode model inherently assumes a monofacial setup, adjustments are required to accommodate the contribution of both faces of a bifacial device. The initial approximation to transform the monofacial model into a bifacial representation involves introducing an equivalent I_{ph} . This equivalent current is derived from the combination of front and rear irradiances [10,12,29]. An alternative representation proposed in [7,10] for bifacial devices involves adapting the single-diode model by connecting two circuits in parallel. In this configuration, one branch represents the frontal face with its respective parameters. In contrast, the other branch represents the rear. The addition of the currents generated in both branches yields I_{pv} . Studies have indicated that the configuration utilizing the equivalent current source exhibits superior performance compared to the parallel configuration [10]. In certain cases, the single-diode model has been further simplified by disregarding resistive effects and eliminating series and shunt resistances [13]. Another formulation extensively used for monofacial PV devices is the double-diode model [30,31], which has also been adapted

to analyze bifacial PV devices. This model has demonstrated remarkable accuracy under standard test conditions (STC) and in various temperature and irradiance conditions [32,33]. The topology of the model closely resembles that of the single-diode model, with an additional diode included in parallel. Incorporating an additional diode into the two-diode model introduces two new parameters, resulting in a formulation with seven parameters. These parameters include photocurrent (I_{ph}), diode ideality factors (n_1, n_2), diode saturation currents (I_{s1}, I_{s2}), series resistance (R_s), and shunt resistance (R_{sh}). Some authors have applied this formulation to bifacial PV devices [8,9]. Other formulations beyond the single and double-diode models have been proposed. In [11], two monofacial electrical models are utilized. The first is an analytical model proposed by Eduardo et al. [34], while the second is an empirical model proposed by King et al. [35]. Both models demonstrated effective performance for non-real-time monitoring, particularly in clear sky conditions, with the analytical model exhibiting greater accuracy compared to the empirical model.

Previously, various models were discussed to elucidate the approaches adopted by different authors representing the electrical characteristics of bifacial PV modules. Among these models, the single-diode model (SDM) stands as a conventional choice. It is depicted in Equation (1), where the current sources symbolize both the frontal and rear sides of the bifacial module. Figure 1 shows a schematic representation of this model.

$$I_{pv} = I_{ph,f} + I_{ph,r} - I_s \left[\exp \left(\frac{V_{pv} + I_{pv} \cdot R_s}{N_s \cdot V_t \cdot n} \right) - 1 \right] - \frac{(V_{pv} + I_{pv} \cdot R_s)}{R_{sh}} \quad (1)$$

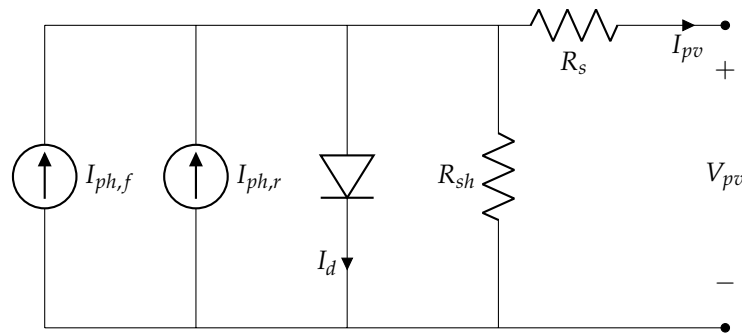


Figure 1. Single-diode model adapted for bifacial PV devices.

An alternative representation of the single-diode model employs two parallel branches, each corresponding to one side of the module. This configuration is illustrated in Figure 2. The resultant current, denoted by I_{pv} in Equation (2) is the sum of Equations (3) and (4).

$$I_{pv} = I_f + I_r \quad (2)$$

$$I_f = I_{ph,f} - I_{s,f} \left[\exp \left(\frac{V_{pv} + I_f \cdot R_{s,f}}{N_s \cdot V_{t,f} \cdot n} \right) - 1 \right] - \frac{V_{pv} + I_f \cdot R_{s,f}}{R_{sh,f}} \quad (3)$$

$$I_r = I_{ph,r} - I_{s,r} \left[\exp \left(\frac{V_{pv} + I_r \cdot R_{s,r}}{N_s \cdot V_{t,r} \cdot n} \right) - 1 \right] - \frac{V_{pv} + I_r \cdot R_{s,r}}{R_{sh,r}} \quad (4)$$

Another commonly employed model is the double-diode model (DDM), as depicted in Equation (5). This formulation introduces an additional diode-current, necessitating the inclusion of two additional terms for I_0 and n . A visual representation is found in Figure 3.

$$I_{pv} = I_{ph,f} + I_{ph,r} - I_{s1} \left[\exp \left(\frac{V_{pv} + I_{pv} \cdot R_s}{N_s \cdot V_t \cdot n_1} \right) - 1 \right] - I_{s2} \left[\exp \left(\frac{V_{pv} + I_{pv} \cdot R_s}{N_s \cdot V_t \cdot n_2} \right) - 1 \right] - \frac{V_{pv} + I_{pv} \cdot R_s}{R_{sh}} \quad (5)$$

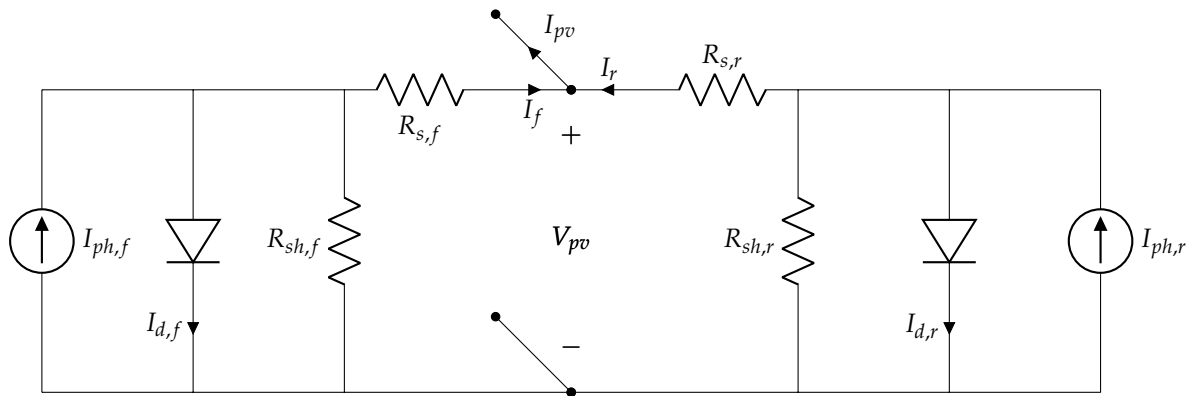


Figure 2. Paralell configuration of the single-diode model for bifacial PV devices.

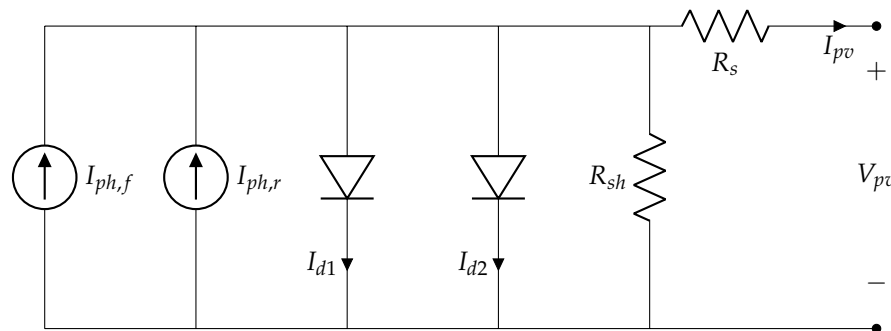


Figure 3. Double-diode model adapted for bifacial PV devices.

3.1. The Bifacial Representation

As previously discussed, various models derive the IV curve and energy production for bifacial PV devices. Regardless of the specific model used, a crucial consideration lies in how these models effectively represent the bifacial nature of the device. Following parameter estimation, decisions must be made regarding each element in the circuit. In the work of [8], for instance, they proposed rescaling the parameters I_{ph} , I_{s1} , I_{s2} , and R_s for both the front and rear faces while neglecting R_{sh} . This rescaling process is accomplished by incorporating the respective frontal and rear irradiances, as shown in Equations (6) and (7).

$$I_{ph(f+r)} = \frac{I_{f,sc} \cdot G_f + I_{r,sc} \cdot G_r}{G_{STC}} \tag{6}$$

$$X = \frac{X_f \cdot G_f + X_r \cdot G_r}{G_f + G_r} \tag{7}$$

where the term X represents I_{s1} , I_{s2} , and R_s . It is important to note that $I_{r,sc}$ is not a parameter found in datasheets. Furthermore, calculating $I_{s1,r}$, $I_{s2,r}$, and $R_{s,r}$ requires data for the rear face, which can be obtained from measurements.

In [9], both single- and double-diode models were implemented. For parameter calculation, they conducted a two-stage optimization process. The current source is determined using the bifaciality factor ($\phi_{I_{sc}}$), as shown in Equation (8):

$$I_{ph(f+r)} = I_{ph}(1 + \phi_{I_{sc}}) \tag{8}$$

Subsequently, a new series resistance, denoted as R_{add} , is introduced to R_s , resulting in a combined series term of $R_s + R_{add} \cdot \phi_{I_{sc}}$. The mathematical representation of the single-diode model is depicted in Equation (9). To incorporate the double-diode model, it simply needs to add the term corresponding to the second diode.

$$I_{pv} = I_{ph}(1 + \phi_{I_{sc}}) - I_{s1} \left[\exp \left(\frac{V_{pv} + I_{pv} \cdot (R_s + R_{add} \cdot \phi_{I_{sc}})}{N_s \cdot V_t \cdot n_1} \right) - 1 \right] - \frac{V_{pv} + I_{pv} \cdot (R_s + R_{add} \cdot \phi_{I_{sc}})}{R_{sh}} \quad (9)$$

In other studies, such as [12], a single-diode model is implemented by considering only the frontal face parameters. As given by Equation (10), the adjustments for bifacial representation involve rescaling the irradiances for the I_{ph} term when parameter extraction is performed under non-STC conditions.

$$I_{ph} = \frac{G_E}{G_{ref}} (I_{ph,ref} + \alpha(T - T_{ref})) \quad (10)$$

Here, G_E is the equivalent irradiance obtained from Equation (11).

$$G_E = G_f + G_r \cdot \phi \quad (11)$$

The subscript “ref” refers to standard test conditions (STC), α represents the temperature coefficient for I_{sc} , and ϕ denotes the bifaciality factor.

In the case of [11], the bifacial behavior is quantified by the “bifacial gain of irradiance”, defined in Equation (12).

$$BG_g = 100 \cdot \frac{G_r}{G_{POA}} (1 - \eta_{loss}) \quad (12)$$

Notably, the authors applied the model to outdoor experimental data, hence the usage of G_{POA} , representing the irradiance in the plane of the array, and η_{loss} , indicating the loss of power due to non-homogeneity in the rear irradiance.

3.2. Models Evaluation

After reviewing the presented models and their respective validations, three have been chosen for a comprehensive evaluation of their performance using experimental data under controlled irradiance and stable temperature conditions. The selection criteria are based on their replicability and the diverse modeling approaches employed. The chosen models are as follows:

- Gu et al. [12] The single-diode model requires 5 parameters. The estimation method the authors proposed for these parameters is implemented as described by Equations (13)–(17).

$$V_{t,ref} = \frac{\beta \cdot T_{ref} - V_{oc,ref}}{\frac{N_s \cdot T_{ref} \cdot \alpha}{I_{ph,ref}} - 3 \cdot N_s - \frac{E_g \cdot N_s}{K \cdot T_{ref}}} \quad (13)$$

$$I_{ph,ref} \approx I_{sc,ref} \quad (14)$$

$$I_{s,ref} = I_{sc,ref} \cdot \exp \left(\frac{-V_{oc,ref}}{N_s \cdot V_{t,ref}} \right) \quad (15)$$

$$R_{sh,ref} = \frac{(V_{mp,ref} - I_{mp,ref} \cdot R_{s,ref})(V_{mp,ref} - N_s \cdot V_{t,ref})}{(V_{mp,ref} - I_{mp,ref} \cdot R_{s,ref})(I_{sc,ref} - I_{mp,ref}) - N_s \cdot V_{t,ref} \cdot I_{mp,ref}} \quad (16)$$

$$I_{mp,ref} = I_{ph,ref} - I_{s,ref} \left[\exp \left(\frac{V_{mp,ref} + I_{mp,ref} \cdot R_{s,ref}}{N_s \cdot V_{t,ref}} \right) - 1 \right] - \quad (17)$$

$$\frac{(V_{mp,ref} + I_{mp,ref} \cdot R_{s,ref})[(V_{mp,ref} - I_{mp,ref} \cdot R_{s,ref})(I_{sc,ref} - I_{mp,ref}) - N_s \cdot V_{t,ref} \cdot I_{mp,ref}]}{(V_{mp,ref} + I_{mp,ref} \cdot R_{s,ref})(V_{mp,ref} - N_s \cdot V_{t,ref})}$$

Once the 5 parameters are calculated, they are adjusted to their actual irradiance and temperature conditions. The photocurrent (I_{ph}) is defined in Equation (10), while the remaining parameters are computed using Equations (18)–(21):

$$I_s = I_{s,ref} \cdot \left(\frac{T}{T_{ref}} \right)^3 \cdot \exp \left[\frac{q \cdot E_g}{k} \left(\frac{1}{T_{ref}} - \frac{1}{T} \right) \right] \quad (18)$$

$$R_s = R_{s,ref} \quad (19)$$

$$R_{sh} = \frac{G_{ref}}{G_E} \cdot R_{sh,ref} \quad (20)$$

$$V_t = \frac{T}{T_{ref}} \cdot V_{t,ref} \quad (21)$$

- Janssen et al. [8] utilizes a double-diode model, where initially 7 parameters have to be estimated. However, based on the author's considerations, 3 parameters are assumed: $R_{sh} = \infty$, $n_1 = 1$, and $n_2 = 2$. Then, to obtain the first diode saturation current, the formulation proposed by [36] is employed, given by Equation (22).

$$I_{s1,ref} = \frac{I_{sc} + \alpha \cdot (T - T_{ref})}{\exp \left(\frac{V_{oc} + \beta \cdot (T - T_{ref})}{n_1 \cdot V_t} \right) - 1} \quad (22)$$

On the other hand, the second diode saturation current is calculated using Equation (23).

$$I_{s2,ref} = \left(\frac{T^{\frac{2}{5}}}{3.777} \right) I_{s1} \quad (23)$$

Finally, the series resistance is calculated using Equation (19). Just I_{ph} and $I_{s,i}$ are transformed to their original ambient conditions; the first is accomplished by applying Equation (6), and the second is accomplished by the application of Equation (24).

$$I_{s(i)} = I_{s(i),ref} \cdot \left(\frac{T_k}{T_{ref}} \right)^3 \cdot \exp \left(\frac{q E_g}{n_i k} \left(\frac{1}{T_{ref}} - \frac{1}{T_k} \right) \right) \quad (24)$$

- Bhang et al. [7] proposed a single-diode model with a parallel configuration, resulting in the estimation of 10 parameters: 5 for the frontal face and the other 5 for the rear. A W-Lambert parameter estimation is employed to obtain it, utilizing the measured values at STC for both faces. Finally, the parameters are corrected utilizing Equations (10) and (18)–(20).

4. Methodology

4.1. Setup

This section describes the equipment utilized for measurements, beginning with PV bifacial modules and then proceeding to the sun simulator.

4.1.1. Bifacial Modules

Table 2 displays the various modules subjected to measurement. Different technologies were employed, with a predominant use of PERC+ and HJT. The last column indicates the specific test to be conducted, which will be elucidated in the subsequent sections. It is worth mentioning that GOPV PSDA6, HET GO 25, and n-PERT modules are frameless, whereas Risen, Trina, and SunPower modules are equipped with frames.

Table 2. Modules utilized for IV curve tracing with the sun simulator.

Manufacturer	Model	Source	$P_{max}(W)$	Technology	Test
Risen	RSM72-6-370BMDG	Santiago, Chile	370	PERC+	SS, DS
CEA-INES HJT 1	GOPV PSDA 6	Antofagasta, Chile	393	HJT	SS
CEA-INES HJT 2	HET GO 25	Antofagasta, Chile	355	HJT	SS
CEA-INES nPERT	n-PERT	Antofagasta, Chile	348	n-PERT	SS
Trina	TSM-490DEG18MC.20(II)	Santiago, Chile	490	PERC+	DS
SunPower	SPR-P6-500-COM-S-BF	Santiago, Chile	500	PERC+	SS, DS

4.1.2. Solar Simulator

The EternalSun sun simulator (A+A+A+ class) is employed to illuminate and trace IV curves for the selected modules. The sun simulator utilizes a single long-pulse filtered xenon tube lamp in the bottom chamber. Consequently, the module and reference cell must be oriented towards the bottom to receive the light. The irradiance levels can be controlled within 100 to 1200 Wm^{-2} .

The upper chamber is mobile, allowing it to be lowered to cover the module completely, preventing the entry of external light. The interior of the upper chamber is black, eliminating any reflection of the emitted light. Once the upper chamber is lowered, temperature control is possible within a range of 10 to 75 °C.

A reference cell is connected to measure irradiance, and within the interior of the bottom chamber, there is another cell named the “monitor cell”, which measures both irradiance and temperature.

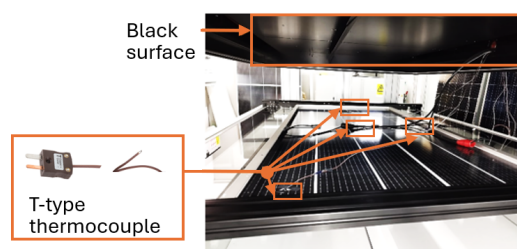
Temperature measurement employs two instruments: the first utilizes four T-type thermocouples, primarily when tracing IV curves at different temperatures, as it allows temperatures above 100 °C. The second is an IR thermal sensor, allowing temperature measurements up to approximately 49 °C.

4.2. Measurement

The following sections describe the two tests conducted, the first one using single-sided illumination and the second one with double-sided illumination.

4.2.1. Single-Sided Illumination (SS)

The PV modules listed in Table 2 underwent the tracing of their IV curves at STC conditions, as depicted in Figure 4. For temperature measurement, four T-type thermocouples are affixed to the module using aluminum foil tape following the method outlined in the standard IEC 60891 [37].

**Figure 4.** Solar simulator setup for single-sided measurement.

4.2.2. Double-Sided Illumination (DS)

For this measurement, a 90% reflective film is applied to cover the surface of the upper chamber. This configuration enables the light emitted from below to be partially reflected by the film, thereby providing additional illumination to the rear side of the bifacial module, as illustrated in Figure 5.

As the reflected light onto the rear surface is not uniform, it becomes crucial to measure the irradiance across the surface of the modules. The modules were virtually divided

into nine sections, marked by the red X symbols in Figure 6. The resulting irradiance distributions are named “irradiance matrix”. Irradiance measurements were conducted with a reference cell positioned in each section. Additionally, an extra point is included below position 2C, which is the reference cell’s position after irradiance measurement. This adjustment helps prevent shadowing on the rear face during IV curve tracing.

With this configuration, the upper chamber remains lifted to maintain reflection onto the surface. In this case, temperature cannot be controlled. However, frontal irradiance can also be regulated, affecting rear irradiance. The module is exposed to irradiances ranging from 100 to 1000 Wm⁻², in 100 Wm⁻² increments. For every data point, the rear irradiance is measured in the position below 2C.

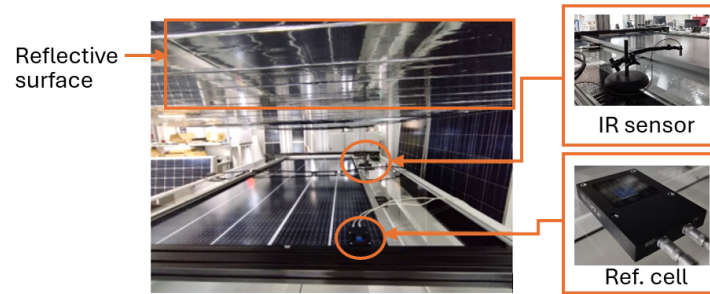


Figure 5. Solar simulator setup for double-sided measurement.

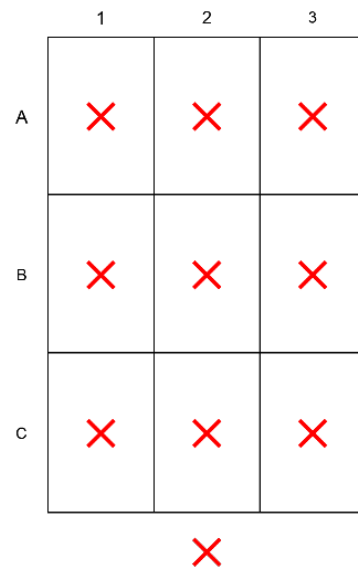


Figure 6. Rear irradiance measuring points to evaluate uniformity in the surface of the module.

4.3. Data Processing and Model Approach

The processing will be divided into two parts, each corresponding to a different test. Among the seven models listed in Table 1, three have been chosen for their replicability, a selection process that will be detailed further below.

4.3.1. Single-Sided Illumination Measurement (SS)

In this measurement, the frontal and rear faces are tested to obtain their respective IV curves for STC conditions. It is important to note that the bifacial models previously discussed cannot be applied here, as two IV curves are traced separately. The primary objective of this test is to examine the behavior of each module face independently and to observe any potential differences between them.

In this scenario, the single-diode model is applied to analyze each IV curve. The standard test condition (STC) measured points (I_{sc} , V_{oc} , I_{mpp} , and V_{mpp}) are employed for both the frontal and rear faces. Subsequently, these data points are inputted into the 5-parameter

model for each face of the module. Following parameter acquisition, the models are used to simulate the IV curves. The comparison between the simulated and experimental IV curves involves calculating percent errors for voltage values, considering I_{sc} for current and P_{max} for power. Figure 7 summarizes every step of this measurement.

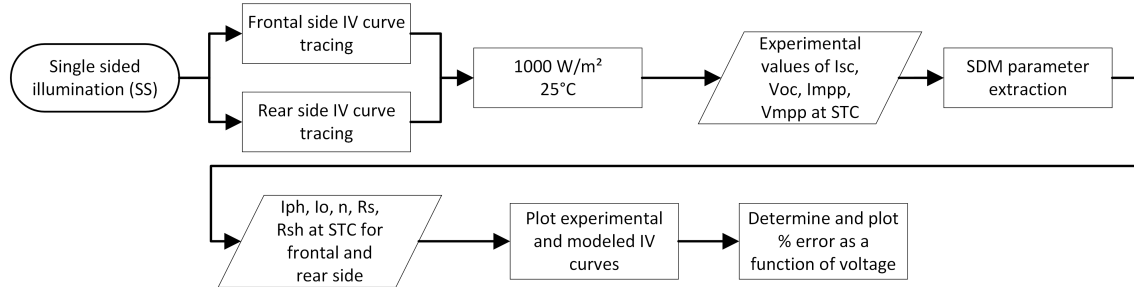


Figure 7. Single-sided illumination measurement explanation scheme.

4.3.2. Double-Sided Illumination Measurement (DS)

In this case, the measured irradiances in Figure 6 are used to determine the minimum irradiance value under the assumption that this value limits the short-circuit current, given that each cell operates as a miniature current source [38]. This minimum value, along with the STC measured points, serves as input for evaluating the proposed models by [7,8,12].

Once the irradiances are measured, the reference cell is located under the 2C position, and IV curves are traced in the range from 100 to 1000 Wm^{-2} for the frontal side. The data used for evaluating the models are the STC data corresponding to I_{sc} , V_{oc} , I_{mpp} , and V_{mpp} , previously obtained by the single-sided illumination measurement.

Analogous to SS measurements, percent errors are calculated by comparing experimental and modeled data to ascertain the model with the best performance. Once this model is identified, it undergoes comparison with direct parameter extraction using IV curves under DS illumination. Subsequently, a sensitivity evaluation is conducted to determine which parameters have the most significant impact on IV curve tracing. This process is illustrated in Figure 8.

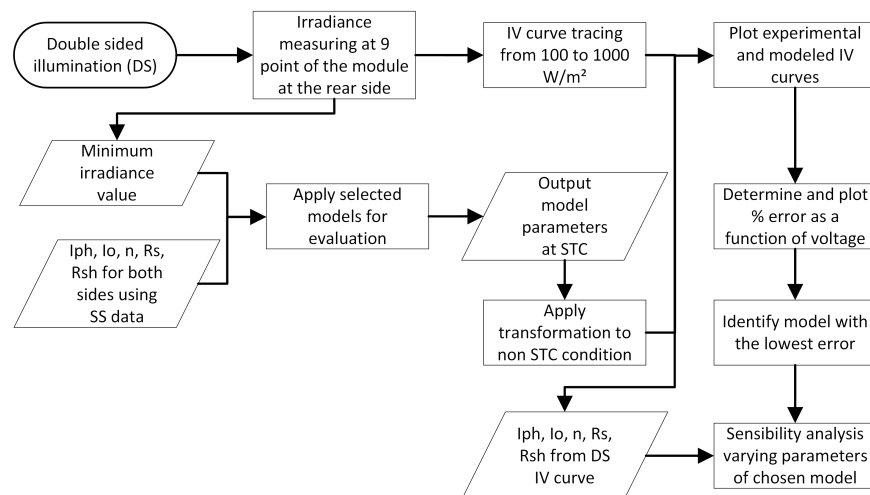


Figure 8. Double-sided illumination measurement explanation scheme.

5. Results and Discussion

The results are divided into two sections: single-sided and double-sided measurements. The best model from the double-sided measurements is then chosen for further parameter evaluation.

5.1. Single-Sided Illumination Measurement

IV curves for the five modules under STC conditions are modeled with the SDM and compared with experimental data. Figures 9a, 10a, 11a, 12a and 13a show the frontal and rear IV curves for each module, while Figures 9b, 10b, 11b, 12b and 13b illustrate the differences between estimated and measured values across the entire IV curve. These differences are particularly noticeable near the maximum power point, with the SunPower module presenting the largest deviations, reaching a percentage error close to 20% on the rear side, while the HET GO 25 module exhibits smaller differences, with a maximum error on the rear side slightly over -2.5% .

Modeling the IV curve under shadow effects poses challenges due to current steps introduced by shadows from the frame and junction box. Most models do not account for these steps, leading to discrepancies. When both sides of the module receive illumination, the error remains minimal because the front side typically receives higher irradiance, reducing the impact of shadowing. However, when only the rear side is illuminated, shadow-induced steps in the IV curve become more pronounced, leading to larger modeling errors.

For instance, at 1000 W/m^2 on the rear side, shadowing from the frames creates visible steps in the IV curve, corresponding to noticeable differences between model predictions and experimental data. In specific cases, such as the SunPower module, additional shadowing from the junction box accentuates these steps, especially near the maximum power point, contributing to the larger discrepancies observed when only the rear side is illuminated. Although this effect might not significantly impact maximum power estimation in tilted configurations, it poses challenges in vertical east-west orientations where both sides could be directly illuminated.

To improve accuracy under partial shading, it is necessary to incorporate shadow effects directly into the model. This requires identifying both the affected areas of the IV curve and the magnitude of current steps caused by shadows. By refining the model to include these variables, IV curve estimation can be enhanced, particularly for configurations prone to shadowing on one or both sides of the module.

For modules with minimal shadowing effects, such as the HET GO25, HJT GOPV PSDA 6, and nPERT, both frontal and rear face IV curves exhibit smaller errors, with current deviations not exceeding $\pm 5\%$ at the maximum difference point, indicating strong agreement between experimental data and model predictions.

Another notable effect appears when analyzing the IV curves for the front and rear sides. First, the V_{oc} values for each side differ, with the rear side generally showing a lower voltage in shaded conditions, as observed in Figures 9a and 10a. This effect is less evident when shadowing steps on the rear side are minimal, as shown in Figures 11a, 12a and 13a. Additionally, shadowing shifts the maximum power point (MPP) position, moving it to the right for the rear side, which is clearly visible in Figures 9b and 10b.

Further research is needed to systematically evaluate the impact of different technologies on model performance, particularly given the notable differences observed among the studied modules. These variations are likely influenced by frame effects and shading on the rear side. Since the front sides of all devices are subject to identical conditions and each side is measured independently, the behavior of the front side can be analyzed with greater precision. Across all modules, the experimental IV curves generally exhibit a more squared shape compared to the modeled curves. In particular, Risen (Figure 9a) and n-PERT (Figure 13a) modules display a markedly squared IV curve relative to the others. This distinct behavior, observed in only some modules of similar technologies, suggests that additional, unaccounted-for factors may be influencing the outcomes. Therefore, these differences cannot be conclusively attributed solely to technology type, underscoring the need for further investigation into these and other possible phenomena.

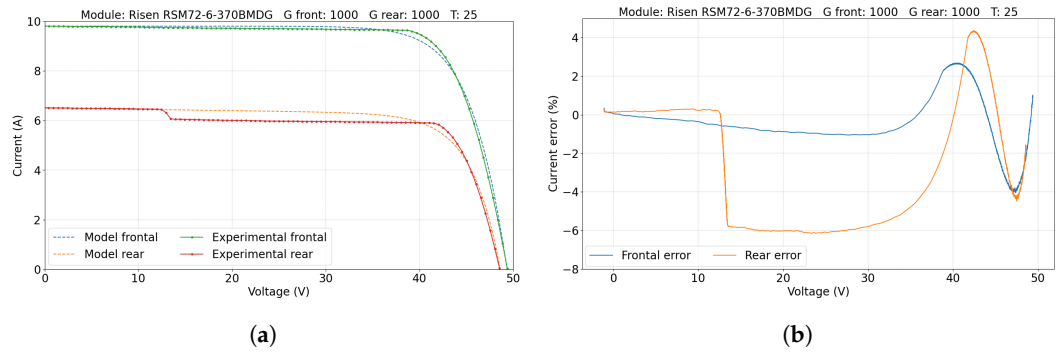


Figure 9. (a) IV curves for frontal and rear faces of Risen RSM72-6-370BMDG and (b) current difference between experimental data and model results.

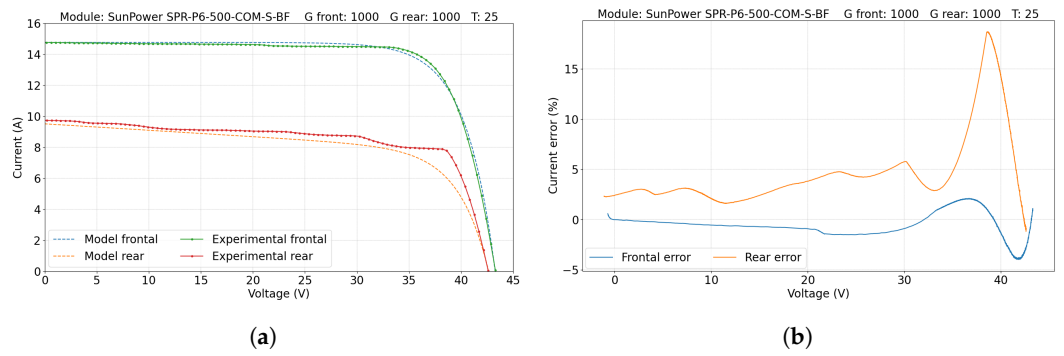


Figure 10. (a) IV curves for frontal and rear faces of SunPower SPR-P6-500-COM-S-BF and (b) current difference between experimental data and model results.

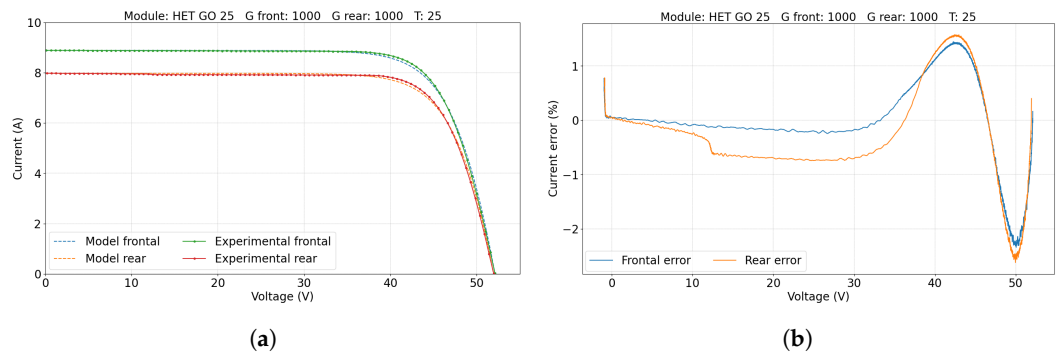


Figure 11. (a) IV curves for frontal and rear faces of HET GO25 and (b) current difference between experimental data and model results.

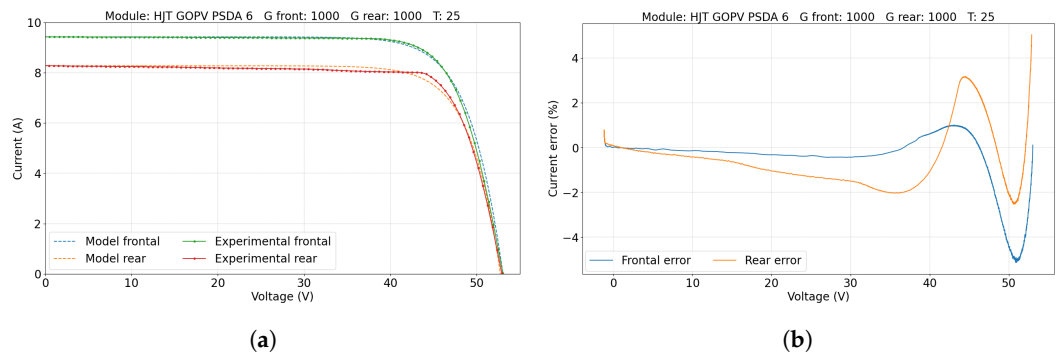


Figure 12. (a) IV curves for frontal and rear faces of HJT GOPV PSDA 6 and (b) current difference between experimental data and model results.

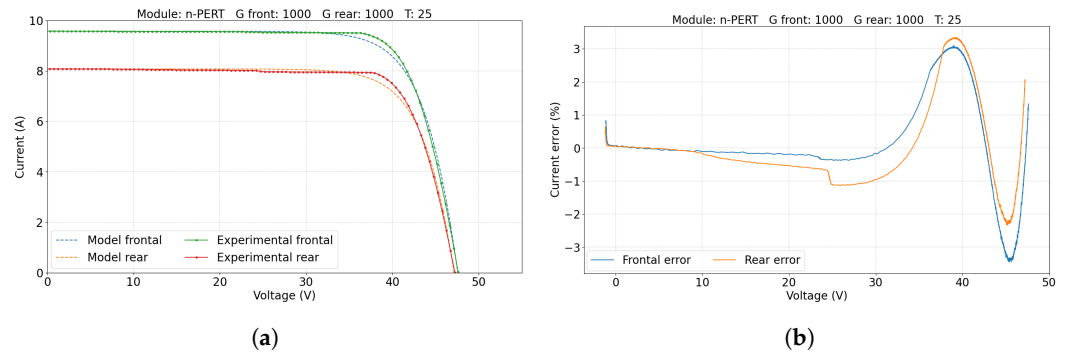


Figure 13. (a) IV curves for frontal and rear faces of n-PERT and (b) current difference between experimental data and model results.

5.2. Double-Sided Illumination Measurement

For this dataset, the three models (Gu et al. [12], Janssen et al. [8] and Bhang et al. [7]) are evaluated and compared with experimental data. IV and PV curves are traced, as seen in Figures 14a, 15a, and 16a, and their respective differences are plotted to identify which one exhibits the minimum and maximum deviations from the experimental data, shown in Figures 14b, 15b, and 16b.

SunPower and Risen modules’ frontal and rear faces were separately tested in the SS measurement. Although both exhibited a gap due to the shadowing effect, their IV curves aligned well in the I_{sc} and V_{oc} regions, with the most significant deviations observed near the maximum power point, which can be seen in the error plots. However, in the bifacial IV and PV curves, while the estimation of I_{sc} closely matched the actual data, deviations appeared as the curves approached the maximum power point and V_{oc} region. Power and current differences between experimental and modeled data were evident for the two mentioned modules, and depending on the evaluated model, this differences can reach values near 100%, which is the case of Bhang et al. [7] model.

When comparing the current and power differences, it was observed that the single-diode model proposed by Gu et al. [12] provided the closest representation of the complete IV curve, which can be seen from the error plots, where the maximum difference is close to 30%. It was followed by Janssen et al.’s [8] double-diode model with parameter escalation by irradiances, which tends to have more differences while approaching the maximum power point and V_{oc} region. Finally, the parallel single-diode model showed poor performance as it tended to underestimate P_{max} and V_{oc} , generating the higher differences at the end of the IV curve caused by the poor voltage estimation.

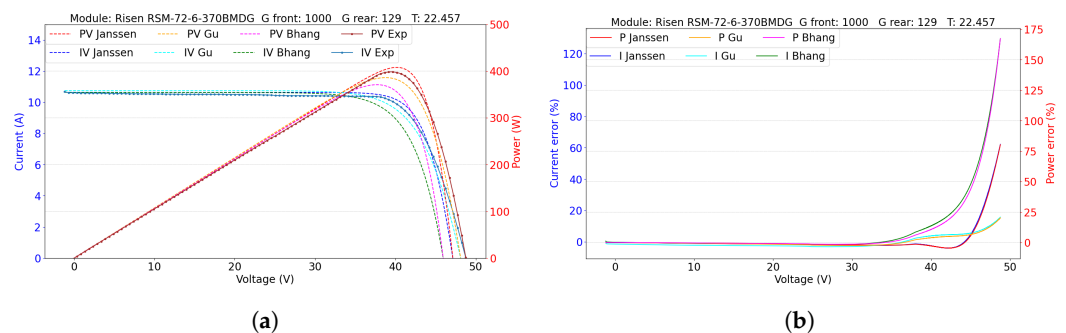


Figure 14. (a) IV and PV curves for experimental and modeled data, an (b) current and power differences between each model and experimental data, illustrated for module Risen RSM72-6-370BMDG.

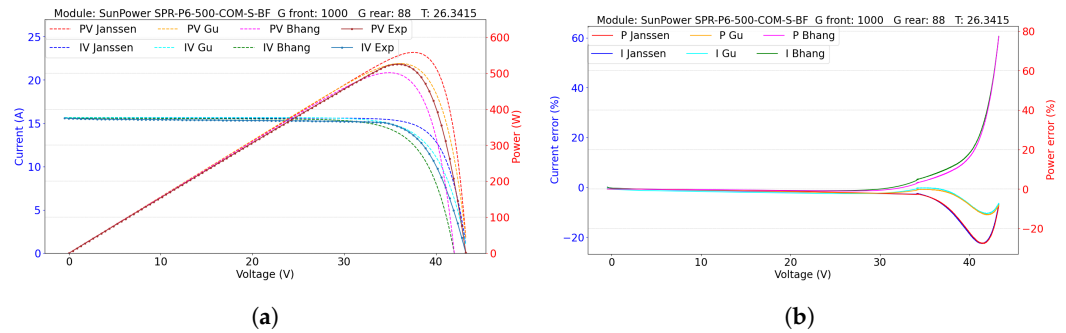


Figure 15. (a) IV and PV curves for experimental and modeled data, an (b) current and power differences between each model and experimental data, illustrated for module SunPower SPR-P6-500-COM-S-BF.

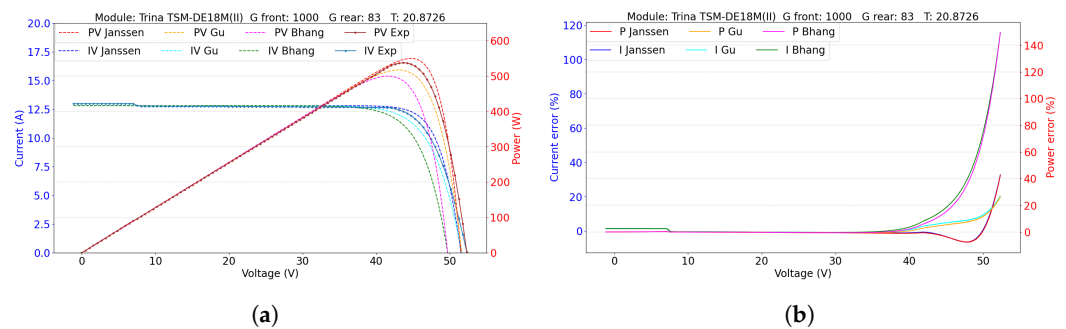


Figure 16. (a) IV and PV curves for experimental and modeled data, an (b) current and power differences between each model and experimental data, illustrated for module Trina TSM-DE18M(II).

From the analyzed behavior when the frontal face is illuminated at 1000 Wm^{-2} , it is noted that the maximum power point and V_{oc} are the two critical points for comparing each model and its fitting with experimental data. To observe what happens at other irradiance points, the difference between modeled and experimental P_{max} , and the difference between the current in the last data point of the plot, is calculated, as shown in Figures 17–19. The evaluation of the models under varying irradiance conditions highlights how each model applies its irradiance correction, a critical factor, as real-world conditions often deviate from STC, with irradiance levels fluctuating from sunrise to sunset. The model by Bhang et al. [7] demonstrates the largest errors in power and current, consistent with prior results, as it tends to underestimate V_{oc} . This underestimation leads to inaccuracies in both current and power at their respective points. Notably, while this model shows lower errors at reduced irradiance levels, the errors increase significantly as irradiance reaches its maximum.

In contrast, the parameter correction by Janssen et al. [8] reveals that the error in P_{max} generally increases with irradiance for the Risen and SunPower modules. However, the Trina module behaves differently, showing reduced error as irradiance approaches maximum levels. This difference suggests that the model does not estimate the maximum power point accurately, creating a gap between curves at this critical point. Regarding current error, it consistently increases across all cases, though the direction (positive or negative) varies depending on whether V_{oc} is overestimated or underestimated.

Finally, the model by Gu et al. [12] displays a more consistent error across varying irradiance levels, maintaining a relatively stable value. This consistency suggests that Gu et al.'s [12] model could be a reliable approach, potentially requiring only minor adjustments to further minimize errors.

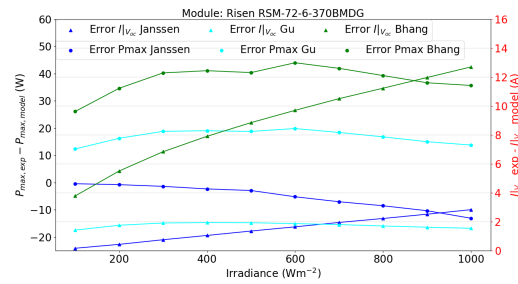


Figure 17. Difference between P_{\max} and current at the last data series point for experimental and modeled data for the Risen RSM-72-6-370BMDG module.

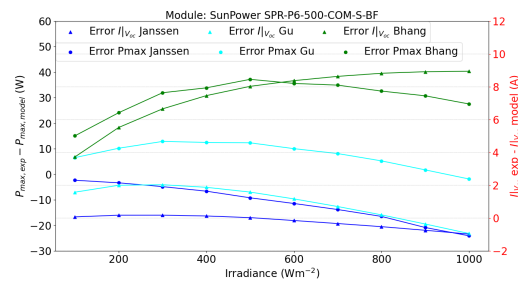


Figure 18. Difference between P_{\max} and current at the last data series point for experimental and modeled data for the SunPower SPR-P6-500-COM-S-BF module.

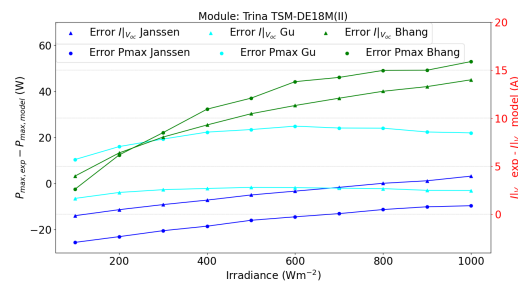


Figure 19. Difference between P_{\max} and current at the last data series point for experimental and modeled data for the Trina TSM-DE 18M(II) module.

Parameters Evaluation

Finally, for a comparison with the parameters calculated from each employed model and the actual IV curve, direct parameter extraction is conducted using experimental data obtained from DS measurements. The obtained parameters are shown in Table 3. Since Bhang et al.'s model utilizes each set of parameters directly estimated, it will not be analyzed in this section.

Gu et al. [12] and Janssen et al. [8] use SDM and DDM, respectively; each obtained parameter is compared with the corresponding model parameter estimation. Each parameter obtained from direct extraction is evaluated in the IV curve, and its respective error when compared with experimental data is calculated and presented in Figures 20–22. It is evident that the errors for both models decreased considerably, considering that Gu et al.'s [12] model reached percent errors above 20% and with direct parameter extraction does not exceed 10%. In the case of Janssen et al.'s [8] model, using their approximations to obtain the DDM parameters, they reached an error higher than 75% in the worst case, while the direct DDM extraction, as well as the SDM extraction, does not exceed 10%.

Gu et al. [12] and Janssen et al. [8] used different methods, SDM and DDM, respectively, to get certain parameters. Each parameter obtained was compared with what the models predicted. Then, these parameters are used to trace the modeled IV curve. Then, the percent error for modeled and experimental IV curves is calculated, shown in Figures 20–22. When direct extraction was applied, errors decreased significantly compared to the models' predictions, considering that Gu et al.'s [12] model reached percent

errors above 20% and with direct parameter extraction does not exceed 10%. In the case of Janssen et al.'s [8] model, using their approximations to obtain the DDM parameters, they reached an error higher than 75% in the worst case, while the direct DDM extraction, as well as the SDM extraction, does not exceed 10%.

Table 3. Parameters obtained from every bifacial model employed and compared with direct extraction using SDM and DDM.

Module	Model	I_{ph}	I_{o1}	I_{o2}	R_s	R_{sh}	n_1	n_2
Risen	SDM parameter extraction	10.5943	$8.9835 \cdot 10^{-7}$	-	0.1415	inf	1.62	-
	Gu et al. [12]	10.7488	$9.3922 \cdot 10^{-7}$	-	0.1638	inf	1.61	-
	DDM parameter extraction	10.5943	$2.4945 \cdot 10^{-7}$	$6.4410 \cdot 10^{-7}$	0.1415	inf	1.50	2.20
	Janssen et al. [8]	10.6366	$4.7612 \cdot 10^{-11}$	$1.2335 \cdot 10^{-10}$	0.1285	-	1.00	2.00
Sun Power	SDM parameter extraction	15.5432	$1.2338 \cdot 10^{-6}$	-	0.0120	inf	1.42	-
	Gu et al. [12]	15.6654	$1.1825 \cdot 10^{-6}$	-	0.0146	inf	1.43	-
	DDM parameter extraction	15.5432	$8.7542 \cdot 10^{-7}$	$2.2680 \cdot 10^{-6}$	0.0200	inf	1.40	2.20
	Janssen et al. [8]	15.5987	$1.0311 \cdot 10^{-9}$	$2.6716 \cdot 10^{-9}$	0.0122	-	1.00	2.00
Trina	SDM parameter extraction	12.9789	$4.7242 \cdot 10^{-7}$	-	0.0223	inf	1.65	-
	Gu et al. [12]	12.8143	$8.2291 \cdot 10^{-8}$	-	0.0817	inf	1.50	-
	DDM parameter extraction	12.9789	$2.7752 \cdot 10^{-7}$	$7.1500 \cdot 10^{-7}$	0.0223	inf	1.60	2.20
	Janssen et al. [8]	12.8116	$7.1552 \cdot 10^{-12}$	$1.8538 \cdot 10^{-11}$	0.0759	-	1.00	2.00

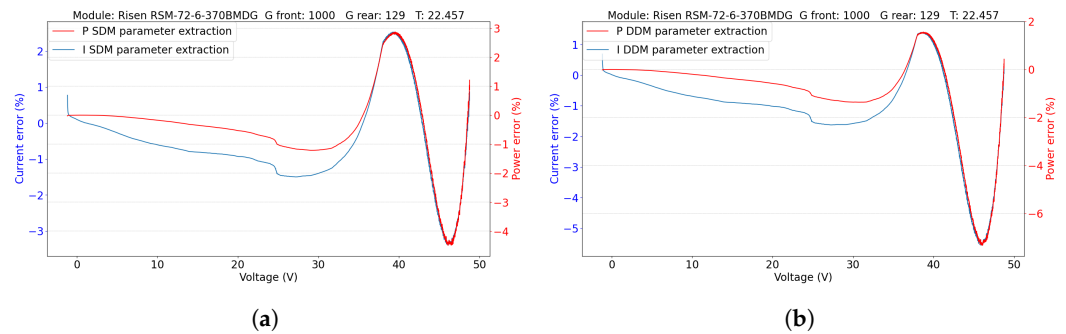


Figure 20. IV and PV curves percent error for direct parameter extraction for (a) SDM (b) DDM for module Risen RSM72-6-370BMDG, considering parameters shown in Table 3.

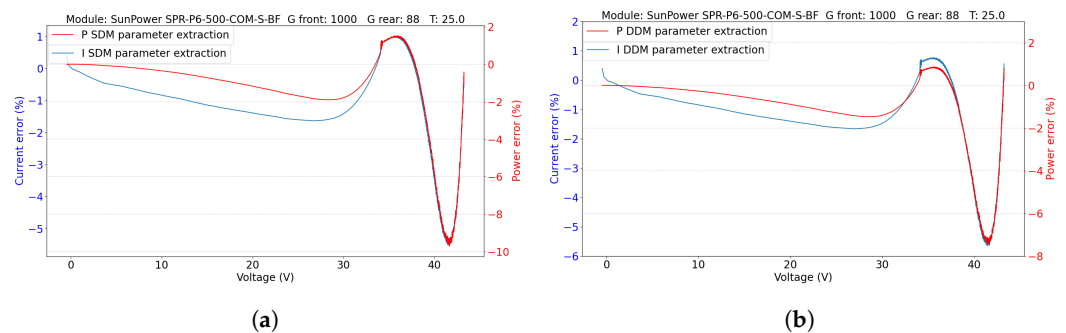


Figure 21. IV and PV curves percent error for direct parameter extraction for (a) SDM (b) DDM for module SunPower SPR-P6-500-COM-S-BF, considering parameters shown in Table 3.

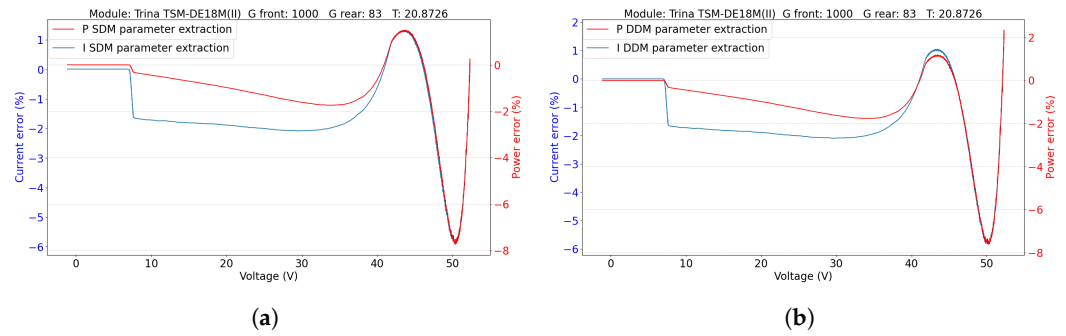


Figure 22. IV and PV curves percent error for direct parameter extraction for (a) SDM (b) DDM for module Trina TSM-DE18M(II), considering parameters showed in Table 3.

From the comparison, it seems that the principal problem associated with Janssen et al.’s [8] model is their parameter estimation for n_1 and n_2 , since they are assumed instead of being calculated. Another difference is the value of I_{o1} and I_{o2} , with 4 magnitude orders of difference. The photocurrent also shows differences; however, they are minimal compared to the effects caused by the use of the other parameters.

On the other hand, since Gu et al.’s [12] model is the one that presents the best performance, it will be subjected to a sensibility analysis of its parameters to identify which one has the greatest impact on its error.

Figures 23–25 illustrate various scenarios wherein each parameter, as derived through the method delineated by Gu, is contrasted with those acquired via SDM parameter extraction from experimental IV curve analysis. The designation “Gu” denotes parameters obtained without any alterations, while “Iph” signifies parameters obtained with the substitution of photocurrent values sourced directly from parameter extraction. Similar designations, namely “Io”, “Rs”, “Rsh”, and “n” denote scenarios wherein all parameters remain consistent with those obtained through Gu’s method, except for the specific parameter indicated in the legend, which is substituted with its SDM-extracted counterpart. Notably, the designation “Est” denotes the error observed when all parameters are derived exclusively through SDM parameter estimation.

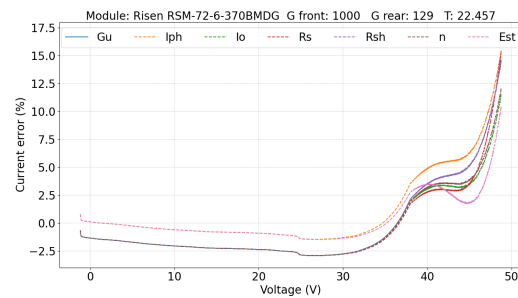


Figure 23. Current error when obtained parameters are changed for the estimated SDM parameters for module Risen RSM-72-6-370BMDG.

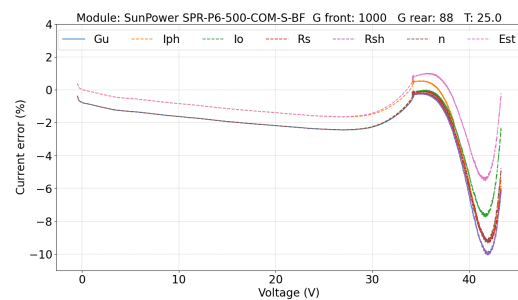


Figure 24. Current error when obtained parameters are changed for the estimated SDM parameters for module SunPower SPR-P6-500-COM-S-BF.

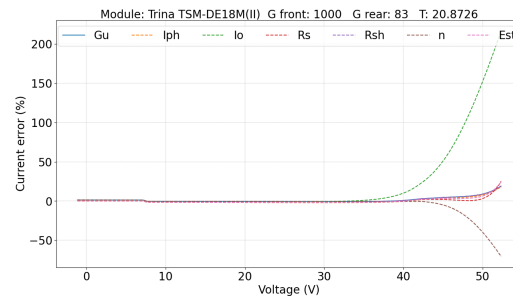


Figure 25. Current error when obtained parameters are changed for the estimated SDM parameters for module Trina TSM-DE18M(II).

The figures presented in Figures 23 and 24 highlight that the most accurate results were achieved through SDM parameter estimation using experimental IV curves. The influence of I_{ph} variations is most pronounced at the onset of the IV curve, which accounts for the near-zero errors observed in the “Iph” and “Est” cases. Conversely, the “Gu” and “Rsh” scenarios exhibit similar behavior, as they both utilize identical parameters due to R_{sh} resulting in ∞ . Subsequently, the most effective substitution leading to minimized errors post SDM parameter estimation involves replacing I_o .

Trina module demonstrates substantial modeling discrepancies compared to other cases due to the sensitivity of its parameters, particularly I_o and n , which influence the IV curve shape significantly. In Figure 25, the replacement of these parameters leads to errors over 50% for n and even surpassing 200% for I_o , highlighting the high impact of these variables on V_{oc} and the overall curve behavior.

The cause of these high errors is evident in the parameter discrepancies detailed in Table 3. For Risen and SunPower modules, extracted parameters using the SDM method align closely with those derived by Gu et al. [12], resulting in minimal divergence. In contrast, the Trina module exhibits larger parameter mismatches: I_o is an order of magnitude smaller; the series resistance is approximately four times lower, and the ideality factor is substantially reduced. These pronounced differences hinder the IV curve’s convergence during parameter adjustments, leading to significant errors, as shown in Figure 25. Consequently, these parameter sensitivities make accurate IV curve modeling for the Trina module particularly challenging.

6. Conclusions

This evaluation of bifacial PV module performance under SS illumination reveals significant shadowing effects from frames and junction boxes, resulting in increased current errors and discrepancies in V_{oc} and P_{max} between frontal and rear IV curves. Further research is essential to understand how different technologies influence model performance, as notable variations among modules indicate the impact of frame effects and rear shading. The experimental IV curves, especially for Risen and n-PERT modules, exhibited a more squared shape compared to the modeled curves, suggesting additional influencing factors. This highlights the need for further investigation beyond technology type alone.

This study compared three models for fitting IV and PV curves: a single-diode model, a parallel single-diode model, and a double-diode model. Among these, Gu et al.’s model (single-diode model) demonstrated the lowest error rates, around 20% at worst. Accurate calculation of the I_o parameter proved crucial for reducing errors, exemplified by SunPower modules, where errors decreased from 10% to 7.5%. In contrast, inaccuracies in I_o estimation for Trina modules resulted in errors exceeding 200%.

This research contributes to existing literature by evaluating modeling techniques using controlled data, thereby minimizing uncertainties in irradiance and temperature. It identifies critical parameters affecting curve accuracy, particularly I_o .

Looking ahead, future research should focus on testing these models in outdoor environments with varying temperatures and irradiance patterns to assess their real-world applicability. Additionally, there is potential to develop innovative methods for accurately

estimating parameters, including the shading effects caused by the frame, to enhance the reliability of PV module modeling.

Author Contributions: Methodology, P.V.-L.; Investigation, P.V.-L.; Data curation, J.G.G.; Writing—original draft, V.G.B.; Writing—review & editing, V.G.B.; Visualization, R.B.; Supervision, P.V.-L. All authors have read and agreed to the published version of the manuscript.

Funding: This research was funded by “Fondo Nacional de Desarrollo Científico y Tecnológico Fondecyt”, number: “11220697” <https://anid.cl/>.

Data Availability Statement: The original contributions presented in the study are included in the article, further inquiries can be directed to the corresponding author.

Acknowledgments: The authors express their gratitude for the financial support from ANID-Fondecyt-11220697, ANID-Fondequip-EQM200183, and VRIIC-USACH. Also, there is financial support from the Scientific Research Initiation Program (PIIC) of the Universidad Técnica Federico Santa María. Finally, our acknowledgments to the Institut National de l’Énergie Solaire CEA-INES in France for their technical support.

Conflicts of Interest: The authors declare no conflicts of interest. The funders had no role in the design of the study; in the collection, analyses, or interpretation of data; in the writing of the manuscript; or in the decision to publish the results.

References

- Mouhib, E.; Micheli, L.; Almonacid, F.M.; Fernández, E.F. Overview of the Fundamentals and Applications of Bifacial Photovoltaic Technology: Agrivoltaics and Aquavoltaics. *Energies* **2022**, *15*, 8777. [\[CrossRef\]](#)
- Cuevas, A.; Luque, A.; Eguren, J.; del Alamo, J. 50 Per cent more output power from an albedo-collecting flat panel using bifacial solar cells. *Sol. Energy* **1982**, *29*, 419–420. [\[CrossRef\]](#)
- Eisenberg, N.P.; Drori, A.; Karsenty, A.; Bordin, N.; Kreinin, L.B. Experimental Analysis of the Increases in Energy Generation of Bifacial Over Mono-Facial PV Modules. In Proceedings of the 26th Europe Photovoltaic Solar Energy Conference Exhibition, Hambourg, Germany, 5–9 September 2011.
- Tina, G.M.; Bontempo Scavo, F.; Merlo, L.; Bizzarri, F. Comparative analysis of monofacial and bifacial photovoltaic modules for floating power plants. *Appl. Energy* **2021**, *281*, 116084. [\[CrossRef\]](#)
- Rodríguez-Gallegos, C.D.; Bieri, M.; Gandhi, O.; Singh, J.P.; Reindl, T.; Panda, S. Monofacial vs bifacial Si-based PV modules: Which one is more cost-effective? *Sol. Energy* **2018**, *176*, 412–438. [\[CrossRef\]](#)
- Tahir, F.; Baloch, A.A.; Al-Ghamdi, S.G. Impact of climate change on solar monofacial and bifacial Photovoltaics (PV) potential in Qatar. *Energy Rep.* **2022**, *8*, 518–522. [\[CrossRef\]](#)
- Bhang, B.G.; Lee, W.; Kim, G.G.; Choi, J.H.; Park, S.Y.; Ahn, H.K. Power Performance of Bifacial c-Si PV Modules with Different Shading Ratios. *IEEE J. Photovoltaics* **2019**, *9*, 1413–1420. [\[CrossRef\]](#)
- Janssen, G.; Van Aken, B.; Carr, A.; Mewe, A. Outdoor Performance of Bifacial Modules by Measurements and Modelling. *Energy Procedia* **2015**, *77*, 364–373. [\[CrossRef\]](#)
- Ahmed, E.M.; Aly, M.; Mostafa, M.; Rezk, H.; Alnuman, H.; Alhosaini, W. An Accurate Model for Bifacial Photovoltaic Panels. *Sustainability* **2023**, *15*, 509. [\[CrossRef\]](#)
- Louw, J. Modelling and Simulation of Bifacial PV Modules by Implementing the Ray Tracing Technique. Master’s Thesis, Stellenbosch University, Stellenbosch, South Africa, 2020. Available online: <https://scholar.sun.ac.za/items/54d3a241-43d1-4654-a4ce-94a7603d132a> (accessed on 1 November 2024).
- Bouchakour, S.; Valencia-Caballero, D.; Luna, A.; Roman, E.; Boudjelthia, E.A.K.; Rodríguez, P. Modelling and Simulation of Bifacial PV Production Using Monofacial Electrical Models. *Energies* **2021**, *14*, 4224. [\[CrossRef\]](#)
- Gu, W.; Ma, T.; Li, M.; Shen, L.; Zhang, Y. A coupled optical-electrical-thermal model of the bifacial photovoltaic module. *Appl. Energy* **2020**, *258*, 114075. [\[CrossRef\]](#)
- Vergura, S. Simulink model of a bifacial PV module based on the manufacturer datasheet. *Renew. Energy Power Qual. J.* **2020**, *18*, 637–641. [\[CrossRef\]](#)
- Lindsay, N.; Libois, Q.; Badosa, J.; Migan-Dubois, A.; Bourdin, V. Errors in PV power modelling due to the lack of spectral and angular details of solar irradiance inputs. *Sol. Energy* **2020**, *197*, 266–278. [\[CrossRef\]](#)
- Antonanzas, J.; Osorio, N.; Escobar, R.; Urraca, R.; de Pison, F.M.; Antonanzas-Torres, F. Review of photovoltaic power forecasting. *Sol. Energy* **2016**, *136*, 78–111. [\[CrossRef\]](#)
- Liang, T.S.; Pravettoni, M.; Deline, C.; Stein, J.S.; Kopecek, R.; Singh, J.P.; Luo, W.; Wang, Y.; Aberle, A.G.; Khoo, Y.S. A review of crystalline silicon bifacial photovoltaic performance characterisation and simulation. *Energy Environ. Sci.* **2019**, *12*, 116–148. [\[CrossRef\]](#)
- IEC TS 60904-1-2:2019; Photovoltaic Devices—Part 1-2: Measurement of Current-Voltage Characteristics of Bifacial Photovoltaic (PV) Devices. Technical Specification. International Electrotechnical Commission: Geneva, Switzerland, 2019.

18. Liang, T.S.; Poh, D.; Pravettoni, M. Challenges in the pre-normative characterization of bifacial photovoltaic modules. *Energy Procedia* **2018**, *150*, 66–73. [CrossRef]
19. Razongles, G.; Sicot, L.; Joanny, M.; Gerritsen, E.; Lefillastre, P.; Schroder, S.; Lay, P. Bifacial Photovoltaic Modules: Measurement Challenges. *Energy Procedia* **2016**, *92*, 188–198. [CrossRef]
20. Lagunas, A.; Cuadra, J.; Petrina, I.; Mayo, M.E. Design of a Special Set-Up for the I-V Characterization of Bifacial Photovoltaic Solar Cells. In Proceedings of the 24th European Photovoltaic Solar Energy Conference and Exhibition, Hamburg, Germany, 21–25 September 2009. [CrossRef]
21. Zhang, Y.; Gao, Q.; Yu, Y.; Liu, Z. Comparison of Double-Side and Equivalent Single-Side Illumination Methods for Measuring the I-V Characteristics of Bifacial Photovoltaic Devices. *IEEE J. Photovoltaics* **2018**, *8*, 397–403. [CrossRef]
22. Abbassi, A.; Mehrez, R.B.; Bensalem, Y.; Abbassi, R.; Kchaou, M.; Jemli, M.; Abualigah, L.; Altalhi, M. Improved Arithmetic Optimization Algorithm for Parameters Extraction of Photovoltaic Solar Cell Single-Diode Model. *Arab. J. Sci. Eng.* **2022**, *47*, 10435–10451. [CrossRef]
23. Hara, S. Parameter Extraction of Single-Diode Model From Module Datasheet Information Using Temperature Coefficients. *IEEE J. Photovoltaics* **2021**, *11*, 213–218. [CrossRef]
24. Piliouguine, M.; Guejia-Burbano, R.; Petrone, G.; Sánchez-Pacheco, F.; Mora-López, L.; de Cardona, M.S. Parameters extraction of single diode model for degraded photovoltaic modules. *Renew. Energy* **2021**, *164*, 674–686. [CrossRef]
25. Rasheed, M.; Alabdali, O.; Shihab, S. A New Technique for Solar Cell Parameters Estimation of The Single-Diode Model. *J. Physics: Conf. Ser.* **2021**, *1879*, 032120. [CrossRef]
26. Rasheed, M.; Shihab, S.; Alabdali, O.; Hassan, H.H. Parameters Extraction of a Single-Diode Model of Photovoltaic Cell Using False Position Iterative Method. *J. Phys. Conf. Ser.* **2021**, *1879*, 032113. [CrossRef]
27. Song, Z.; Fang, K.; Sun, X.; Liang, Y.; Lin, W.; Xu, C.; Huang, G.; Yu, F. An Effective Method to Accurately Extract the Parameters of Single Diode Model of Solar Cells. *Nanomaterials* **2021**, *11*, 2615. [CrossRef] [PubMed]
28. Petrone, G.; Ramos-Paja, C.A.; Spagnuolo, G. *Photovoltaic Sources Modeling*; Wiley & Sons: Hoboken, NJ, USA, 2017.
29. Raina, G.; Sinha, S. A holistic review approach of design considerations, modelling, challenges and future applications for bifacial photovoltaics. *Energy Convers. Manag.* **2022**, *271*, 116290. [CrossRef]
30. Abbassi, A.; Ben Mehrez, R.; Touaiti, B.; Abualigah, L.; Touti, E. Parameterization of photovoltaic solar cell double-diode model based on improved arithmetic optimization algorithm. *Optik* **2022**, *253*, 168600. [CrossRef]
31. Hejri, M.; Mokhtari, H.; Azizian, M.R.; Ghandhari, M.; Söder, L. On the Parameter Extraction of a Five-Parameter Double-Diode Model of Photovoltaic Cells and Modules. *IEEE J. Photovoltaics* **2014**, *4*, 915–923. [CrossRef]
32. Ortiz, S.; Robles, C.; Tobón, J.; Ospino, A.; Martínez, A. Evaluación del desempeño de los modelos de un diodo y dos diodos para módulos fotovoltaicos. *Rev. Espac.* **2020**, *41*, 152–170.
33. Alrahim Shannan, N.M.A.; Yahaya, N.Z.; Singh, B. Single-diode model and two-diode model of PV modules: A comparison. In Proceedings of the 2013 IEEE International Conference on Control System, Computing and Engineering, Penang, Malaysia, 29 November–1 December 2013; pp. 210–214. [CrossRef]
34. Ortiz-Rivera, E.; Peng, F. Analytical Model for a Photovoltaic Module using the Electrical Characteristics provided by the Manufacturer Data Sheet. In Proceedings of the 2005 IEEE 36th Power Electronics Specialists Conference, Dresden, Germany, 16 June 2005; Volume 2005, pp. 2087–2091. [CrossRef]
35. Kratochvil, J.A.; Boyson, W.E.; King, D.L. *Photovoltaic Array Performance Model*; Sandia National Laboratories: Albuquerque, NM, USA, 2004. [CrossRef]
36. Babu, B.C.; Gurjar, S. A Novel Simplified Two-Diode Model of Photovoltaic (PV) Module. *IEEE J. Photovoltaics* **2014**, *4*, 1156–1161. [CrossRef]
37. IEC 60891:2021; International Electrotechnical Commission. Photovoltaic Devices-Procedures for Temperature and Irradiance Corrections to Measured I-V Characteristics. IEC: Geneva, Switzerland, 2021. <https://webstore.iec.ch/en/publication/61766>.
38. Raina, G.; Sinha, S. A comprehensive assessment of electrical performance and mismatch losses in bifacial PV module under different front and rear side shading scenarios. *Energy Convers. Manag.* **2022**, *261*, 115668. [CrossRef]

Disclaimer/Publisher's Note: The statements, opinions and data contained in all publications are solely those of the individual author(s) and contributor(s) and not of MDPI and/or the editor(s). MDPI and/or the editor(s) disclaim responsibility for any injury to people or property resulting from any ideas, methods, instructions or products referred to in the content.